ACS APPLIED ENERGY MATERIALS

www.acsaem.org Article

Unraveling the State of Charge-Dependent Electronic and Ionic Structure–Property Relationships in NCM622 Cells by Multiscale Characterization

Albina Jetybayeva,[¶] Nino Schön, Jimin Oh, Jaegyu Kim, Hongjun Kim, Gun Park, Young-Gi Lee, Rüdiger-A. Eichel, Karin Kleiner,* Florian Hausen,* and Seungbum Hong*

Cite This: *ACS Appl. Energy Mater.* 2022, 5, 1731–1742 Read Online

ACCESS | Metrics & More | Article Recommendations | Supporting Information

ABSTRACT: $LiNi_{0.6}Co_{0.2}Mn_{0.2}O_2$ (NCM622) undergoes crystallographic and electronic changes when charging and discharging, which drive the cathode material close to or even beyond its stability window. To unravel the charge compensation mechanism of NCM622, spatially resolved atomic force microscopy (AFM) measurements in electrochemical strain microscopy (ESM) and conductive AFM (C-AFM) modes are obtained, and the spectroscopic information and crystallographic information are compared. All experiments are performed with two sets of samples: state-of-the-art samples that are composed of a binder, a conductive additive, and an active material and polished samples for single-particle analysis. Near-edge X-ray absorption fine structure spectroscopy shows that ionic Ni^{2+} reacts to give Ni^{3+} when charging and forms covalent bonds with its oxygen neighbors. A Ni^{2+}/Ni^{3+} gradient across the particles balances out with the increasing state of charge, as verified by ESM. Therefore, the results also provide an important view that improves the mechanistic understanding of ESM in electrode materials. Finally, the interplay between the electronic and ionic conductivities and the crystallinities of NCM622 cathodes is elaborated and discussed.

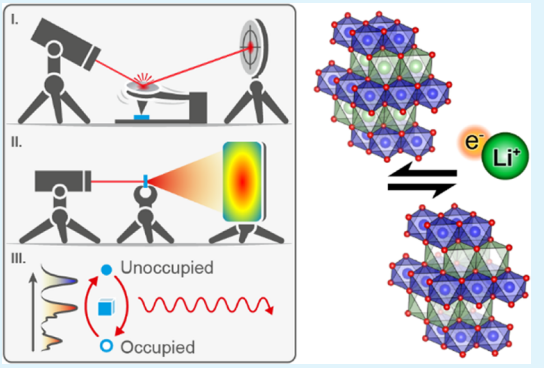

KEYWORDS: *NCM622, state of charge, electrochemical strain microscopy, conductive atomic force microscopy, near-edge X-ray absorption fine structure spectroscopy*

1. INTRODUCTION

A significant increase in the energy demand and drastic climate changes have driven the development of renewable power sources. Energy storage systems such as Li-ion batteries are a key technology to reduce greenhouse gas emissions in the transport sector because of an outstanding well-to-wheel efficiency of up to 70%, a compact design, and exceptional specific and volumetric energy densities.[1−3]

Although the electric vehicle market is rapidly growing,[2,3] the limited range and charging time of Li-ion batteries are still challenging.[4,5] The energy density and kinetic limiting component is the cathode, and in most commercial batteries, lithium transition metal oxides ($LiMeO_2$, Me = Ni, Co, and Mn) have a rhombohedral crystal lattice.[4,6−8] Ni-rich rhombohedral layered oxides ([Ni]/([Ni]+[Mn]+[Co]) ratio ≥0.6) offer the highest energy densities with specific capacities of 175−210 mAh/g at discharge rates of 0.2−1 C and cutoff voltages of 3.0 and 4.3 V.[8−13]

As a higher Ni content results in a better performance and higher capacities, cathodes such as NCM622 (60% Ni) and NCM811 (80% Ni) have been commercialized and have become promising materials for automotive applications.[11,14]

This work focuses on NCM622 as it is well-explored, its specific capacity of 160−200 mA h/g is quite promising, and it demonstrates good thermal stability.[14,15] Furthermore, Cui *et al.* revealed that among NCM (111), (422), (523), (525), and (71515), NCM 622 had the highest diffusivity.[16] Therefore, NCM622 with its excellent electrochemical properties has the potential to be used extensively in Li-ion batteries for various applications such as the emerging automotive sphere.

Kinetic limitations are often determined using pulse techniques such as impedance spectroscopy, galvanostatic or potentiostatic intermittent titration techniques, charge−discharge pulses at distinct states of charge (SOCs), or simple rate tests.[17−20] The as-determined diffusion coefficients of Ni-rich layered oxides are in the range of 10^{-15} m^2 s^{-1}.[18,20,21] However, the discrimination among the ionic and electronic conductiv-

Received: October 10, 2021
Accepted: January 13, 2022
Published: January 24, 2022

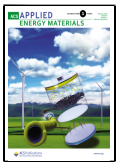

ities, spatially resolved conductivities, and energy density and kinetic limiting factors are hardly known due to the missing links between the available characterization techniques.[6,22,23]

An atomic force microscope operated in different modes can be used to reveal the spatially resolved properties of electrodes, that is, the ionic and electronic conductivities of the layered oxides.[24−27] Electrochemical strain microscopy (ESM), for example, allows the study of electrical properties such as electrochemical strain across particles and electrodes, the distribution of Li ions, and ionic mobility.[28−30] Applying a bias to the atomic force microscope tip thereby induces Li-ion diffusion, resulting in a local electrochemical strain.[27,28] Conductive atomic force microscopy (C-AFM) can be used to study the changes in the electrical properties at different SOCs, which measures the current at a bias voltage applied between a sample and the conductive tip and determines the local electronic conductivity.[31] The results of both ESM and C-AFM provide important information about the local ionic and electronic conductivities of the samples on various scales and at different SOCs. Moreover, different methods of sample preparation enable studying the matrix effects of a binder, conductive carbon, and active material.

The present work aims to unravel the electronic and ionic properties of cathode materials at different SOCs using correlative techniques such as ESM, near-edge X-ray absorption fine structure (NEXAFS) spectroscopy, synchrotron X-ray powder diffraction (SXPD), the galvanostatic intermittent titration technique (GITT), and C-AFM. $LiNi_{0.6}Co_{0.2}Mn_{0.2}O_2$ (NCM622) is studied as a state-of-the-art cathode material to reveal the spatially resolved conductivities of the active material, binder, and conductive carbon using different AFM modes. Time-resolved SXPD and soft NEXAFS spectroscopy are applied to correlate the crystallographic and electronic changes of the samples to the AFM data.

2. EXPERIMENTAL SECTION

2.1. Electrochemical Cycling and Sample Preparation. *2.1.1. Cumulative (Unpolished) Samples.* The slurry of the cathode of unpolished cumulative samples was composed of three materials: active material $LiNi_{0.6}Co_{0.2}Mn_{0.2}O_2$ (NCM622, L&F), electron conductor Super-P (Timcal), and binder polyvinylidene fluoride (PVDF). The three components exhibited a wt % ratio of 94:3:3, which were prepared using *N*-methyl-2-pyrrolidone (NMP). Correspondingly, the slurry for the anode electrode was composed of two materials: an active component (natural graphite, BTR) and a binder (carboxymethylcellulose and styrene-butadiene rubber). The anode slurry was prepared in deionized water with a wt % ratio of 97.4:2.6. Then, the electrode slurries were cast on the surfaces of 15 μm Al (cathode) and 14 μm Cu (anode) current collectors using a doctor blade. Subsequently, they were dried at 100 °C for 12 h. After drying, the load level was maintained at 14.0 mg/cm^2 for the cathode and 9.1 mg/cm^2 for the anode. The N/P ratio, which is the areal capacity ratio of the anode to cathode, was kept at 1.23.

The prepared cathode (NCM622) and anode (natural graphite) were cut to φ14 (diameter of 14 mm). Then, 2032 coin cells were assembled with the electrodes and a φ16 (diameter of 16 mm) polyethylene separator. A solution of 1.15 M $LiPF_6$ dissolved in a mixture of ethylene carbonate (EC) and ethyl methyl carbonate (EMC) at a volume ratio of 3:7 (Enchem Co., Ltd.) was used as the electrolyte (approximately 400 μL per cell). The assembly process was performed in a dry room with a dew point below −50 °C. In total, 18 (nine cathodes and nine anodes for nine cells) samples were prepared and electrochemically tested based on the different parameters.

The prepared cells, except the pristine electrode samples, were first charged and discharged at a *C* rate of 0.1 C (assuming a total capacity of 150 mA h/g) to form a solid−electrolyte interphase (SEI). All cycles were conducted in the voltage range between 3 and 4.2 V. To stabilize the SEI, they were cycled three more times at a 0.2 C rate. Thereafter, the samples were cycled at 0.3 C, and their various states were analyzed. The samples of the first cycle after the SEI formation process were taken at SOCs of 0%, 50% (75 mA h/g), and 100% (150 mA h/g) when charging and at SOCs of 50% (75 mA h/g) and 0% when discharging. All the abovementioned charge−discharge tests were implemented using a galvanostatic cycler (Toscat 3000, Toyo Systems). The cycled cells were then disassembled, rinsed with dimethyl carbonate, and left for 12 h in a vacuum oven for further characterization.

2.1.2. Polished Samples. Electrode preparation of the polished samples was performed using 92.5 wt % cathode material (powder), 4 wt % Timcal Super C65, 3.5 wt % PVDF (Solef), and 6.5 mg of NMP as the solvent. The slurry was casted on an Al foil and dried at 80 °C to obtain a mass loading of approximately 14 mAh/g. Next, the samples with a diameter of 11 mm were punched out of the dried electrodes, and the obtained samples were dried in a Büchi oven (10^{-3} mbar, 120 °C) prior to assembly. The batteries were assembled in an argon-filled glovebox using Swagelok cells with two glass-fiber separators (diameter of 11 mm, glass microfiber 691, VWR, Germany), 60 μL of LP57 (1 M $LiPF_6$ in EC/EMC, 3:7 by weight, <20 ppm H_2O, BASF SE, Germany), and lithium as the counter electrode (diameter of 11 mm, 99.9%, Rockwood Lithium, United States). Five NCM622 (BASF SE, Germany) *versus* Li cells were charged and discharged at 0.05 C (theoretical capacity of 180 mAh/g) to SOCs of 100, 50, and 0%, corresponding to 180, 90 ,and 0 mAh/g (3.0−4.3 V), respectively. After cycling, the cells were disassembled in an argon-filled glovebox. To achieve smooth surfaces for the AFM measurements, the NCM samples were polished. The NCM622 layer remained attached to the Al current collector and was fixed between two copper blocks using a clamp, as illustrated in Figure S1. This setup ensured that a cross-section of the electrode was exposed. The samples were embedded in epoxy resin (EpoFix), subsequently ground, and polished with Al plates contacting the bottom. Figure S2 demonstrates the rate performance, capacity, and cycling efficiency of NCM622.

Figure S3 summarizes the detailed conditions of all the samples (unpolished and polished samples) used for the ESM measurements. White circles show the measurements of the unpolished, cumulative samples, whereas the black circles correspond to the experiments performed with the polished samples.

2.2. AFM and X-Ray Analysis. For the ESM and C-AFM measurements, the same cantilevers (EFM, NanoWorld AG, Switzerland) with a conductive Pt/Ir coating, a nominal force constant of 2.8 N/m, and a nominal resonance frequency of 75 kHz were used and calibrated individually. Slow scanning speeds between 0.1 and 0.5 Hz were chosen to ensure reliable tip−sample interaction. The amplitude results were normalized with respect to the resonance peak Q-factor and drive amplitude for each individual sample, and the corrected amplitude is referred to as the "ESM amplitude" in the figures.

All the measurements of the unpolished cathode material were obtained by employing a commercially available atomic force microscope (Cypher ES model, Asylum Research, USA) at room temperature in an ambient environment. For the ESM measurements, the dual AC resonance tracking piezoresponse force microscopy (DART-PFM) mode was used, which is equivalent to the DART-ESM mode. DART-ESM mapping was conducted with a drive amplitude of 2 V and a loading force of 50 nN. For each sample, at least 10 different places were measured for the statistical analysis. The scan size was kept at 5 × 5 μm^2, the same as that for the scanning electron microscopy (SEM) images (Figure S4).

For measuring the polished NCM material, a commercially available atomic force microscope (Bruker, Santa Barbara, USA, Dimension Icon Microscope) operating inside a glovebox (MBraun, Stratham, USA, O_2 < 0.1 ppm, H_2O < 0.1 ppm) was used. On the Bruker system, the contact resonance frequency (CRF) and amplitude were tracked using a phase-locked loop (HF2LI, Zurich Instruments, Switzerland). The applied drive amplitude and normal load were 4 V

https://doi.org/10.1021/acsaem.1c03173
ACS Appl. Energy Mater. 2022, 5, 1731−1742

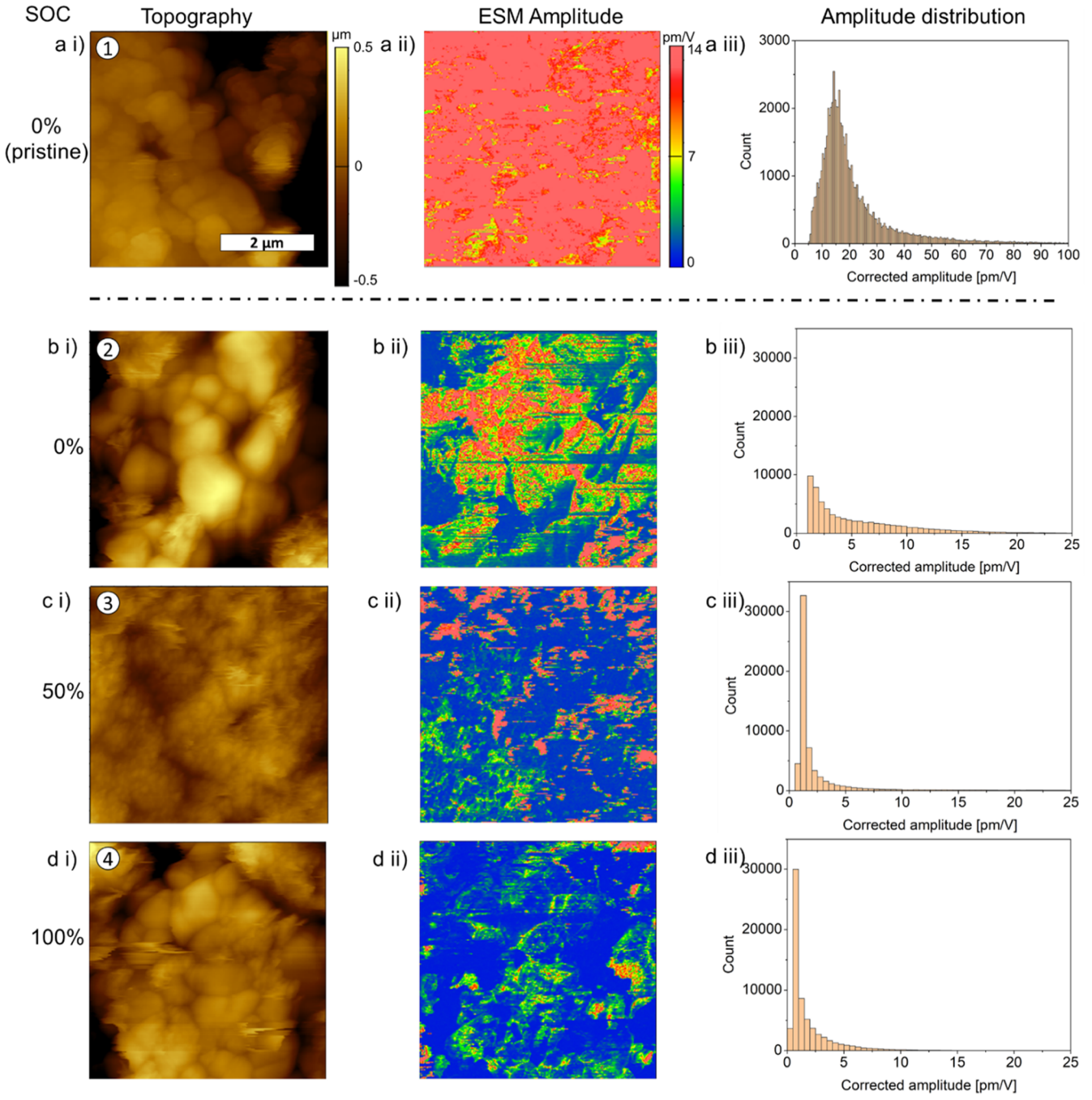

Figure 1. Topography (i) and ESM amplitude (ii) mappings of NCM622 electrodes as well as the corresponding histograms (iii) in (a) the pristine state, (b) at 0% SOC, *i.e.*, fully lithiated, after four SEI formation/stabilization cycles, (c) at 50% SOC, and (d) at 100% SOC, that is, fully delithiated. While the topography does not show significant variations at different SOCs, the ESM amplitude varies significantly as a function of the SOC, and this result is visible in the histograms.

and 56 nN, respectively. For each sample, multiple NCM particles were analyzed. The CRF between the samples and tip was observed to be between 300 and 390 kHz. Both the topographical and amplitude signals were obtained simultaneously.

To investigate the electronic conductivity of the different samples, the C-AFM mode was implemented using an ES dual gain cantilever holder (ORCA, Asylum Research, USA) and an EFM cantilever with a conductive Pt/Ir coating and a force constant of 2.8 N/m (NanoWorld AG, Switzerland). All of the measurements were performed with a controlled loading force of 55 nN with a bias of 1 V applied to the samples. At least five images of the current distribution on the different regions were recorded for the statistical analysis. For the C-AFM measurements performed on the polished samples, a DC bias of 4 V was applied to the sample. The cantilevers used were CONTPt from Nanosensors (Switzerland) with a nominal force constant of 0.2 N/m and a Pt/Ir coating. The average current was calculated solely for areas that were identified as NCM particles in the topography.

Time-resolved operando SXPD of the first NCM622/Li cycle [samples (I–III)] was performed at beamline I11 (Diamond Light Source, UK) using the position sensitive detector of the beamline.[29] The energy of the X-ray beam was 25 keV, which corresponds to a calibrated wavelength of 0.489951(10) Å. The batteries were mounted on an xyz-stage, and each cell was adjusted to the center of diffraction. The cells were cycled at C/3 between 3.0 V and 4.3 V at room temperature. The 2D data were refined using the software

https://doi.org/10.1021/acsaem.1c03173
ACS Appl. Energy Mater. 2022, 5, 1731−1742

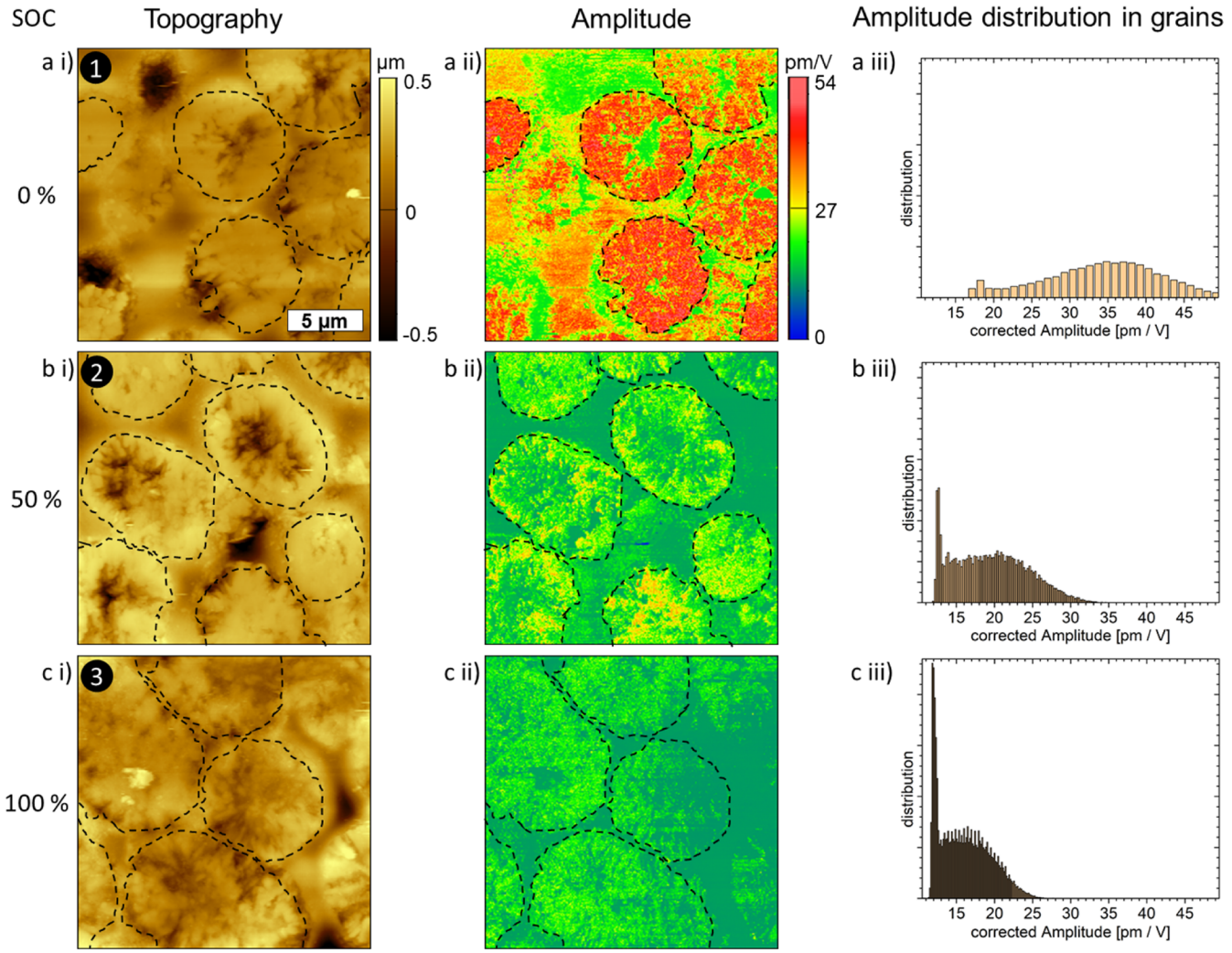

Figure 2. Topography (i) and ESM amplitude (ii) mappings of NCM622 embedded in epoxy glue and polished as well as the corresponding histograms (iii) of the ESM amplitude of marked NCM622 particles at different SOCs: (a) 0% SOC, (b) 50% SOC, and (c) 100% SOC, as measured on the first discharge (see Figure S3 for the cycling history of the samples).

package Fullprof (2θ range: 0−65°). Al (current collector) and Li (counter electrode) showed preferential orientations; therefore, the phases were included in the refinements using the Le Bail method.

NEXAFS measurements of Ni $L_{2,3}$, Co $L_{2,3}$, Mn $L_{2,3}$, and O K of the polished samples were carried out in fluorescence yield (FY) detection mode at the Karlsruhe synchrotron light source KARA (Germany). The photon energy resolution was set to 0.2−0.4 eV, and energy calibration (using a NiO reference), dark current subtraction, division by I_0, background subtraction, data normalization, and absorption correction were performed.[23,32,33]

3. RESULTS AND DISCUSSION

The long-term performance of NCM622, which includes the rate performance, capacity, and cycling efficiency, is shown in Figure S2a. After 82 cycles, the cathode material shows a capacity retention of 94%. The discharge capacity of the second cycle is 182 mAh g^{-1} with two dq/dV peaks at approximately 3.7 V (Figure S2b,c) upon charge (positive y-axis) and discharge (negative y-axis). During cycling, Li ions are reversibly deintercalated/intercalated from/into the NCM622 host structure, while electrons are extracted/inserted, which requires the material to have good electronic and ionic conductivities at the same time.

ESM is sensitive to the mobility of ionic charge carriers and the number of mobile Li ions; therefore, this technique can capture a more complete picture of the mobility of Li^+ in NCM622.[28,30,34−37] Figure 1 shows the topography as well as the simultaneously recorded ESM amplitude signal of the NCM622 electrodes at various SOCs. Note that these samples contain a binder (PVDF) and conductive carbon (C65) and have not been polished after electrochemical cycling; therefore, the signal is composed of contributions from both the active NCM material and the inactive matrix to the signal. A rather high and homogeneous ESM amplitude signal is observed for the pristine state before electrochemical cycling (Figure 1a). A significantly lower ESM signal that shows an overall decay and a more heterogeneous distribution is found with the increasing SOC [measured after four initial cycles between 3 V and 4.2 V in a graphite||NCM622 cell, that is, after the formation of the cathode−electrolyte interphase (CEI)].[38,39] A detailed scheme of the experimental procedure and nomenclature of the samples as well as a correlation of the topography shown in the AFM images with SEM images is presented in the Supporting Information (Figures S3 and S4, respectively). Figure 1 reveals that the signal mainly covers an NCM particle, although it is evident that next to the NCM particle, clear ESM

https://doi.org/10.1021/acsaem.1c03173
ACS Appl. Energy Mater. 2022, 5, 1731−1742

amplitude values arise from the supporting matrix. This signal can be attributed to PVDF being piezoelectric and interfering with the applied ESM bias.

To reveal the spatially resolved changes depending on the SOC of only the NCM622 particles, polished electrode cross-sections were probed on a larger scale (scan size of 20 × 20 μm^2), as illustrated in Figure 2. Due to the polishing, a bare NCM622 surface faces the AFM tip, allowing us to probe only the active material.

Individual NCM particles embedded in the binder are clearly identified and encircled for all SOCs. Such a classification is especially based on the clear difference between NCM and the surrounding matrix in the ESM amplitude signal and is less obvious in the topography, validating a previous study that observed a significantly weaker amplitude signal for piezoelectric materials than that for ionic materials.[40]

A very similar overall behavior to the cumulative NCM and binder signal shown in Figure 1 is observed, proving that even if the particles are embedded in a binder/conductive carbon matrix, the observed trends can be associated with the active material. The majority of the discharged NCM622 signals (0% SOC) show a relatively high amplitude with a broad distribution [Figure 2a(iii)]. The results in Figure 2 exhibit a strong gradient in the ESM signal across the NCM622 particles, and boundary regions show much higher amplitudes than the bulk material.

The high amplitudes are assumed to account for the overall high Li concentration within the pristine/discharged samples, while the broad width of the signal, as shown in the histogram, implies a very inhomogeneous Li concentration within the particles. However, in pristine or discharged NCM622 (x = 1 in $Li_xNi_{0.6}Co_{0.2}Mn_{0.2}O_2$), hardly any Li vacancies are present, which are needed for Li migration throughout the bulk structure (hopping mechanism). Therefore, the Li diffusion coefficient is relatively small at low SOCs, which is proven by the GITT measurements (Section 2, Supporting Information).

The migration of Li ions while applying an electric field between the AFM tip and current collector is assumed to be the origin of the ESM signal, but given the poor ionic conductivity in the absence of Li vacancies, the observed high signal is rather unexpected; notably, a clear correlation between the amount of Li in the Me−O host structure and the amplitude of the signal has been observed earlier[30] and is discussed in more detail further. When charging (Figure 2b: 50% SOC and Figure 2c: 100% SOC), the amplitude distributions narrow, and the maximum signal decreases.

Figure 3a shows the corrected ESM average amplitude of the NCM622 samples as a function of the SOC. As a general trend, the ESM signal decreases from the discharged state to the charged state, that is, from a high overall Li content to a lower overall Li content within the cathode material. At first glance, this seems to support the correlation between the amount of Li ions present and the ESM signal. Regarding the unpolished cumulative active material and binder samples, the pristine, fully lithiated material exhibits the highest ESM amplitude. This value is not reached again after charging and discharging, which is attributed to the formation of the CEI, accompanied by a decreased amount of mobile or active Li ions due to either the total amount of Li ions decreasing or a change in the oxidation states (the electronic structure).[41−44]

Although a direct comparison between the obtained ESM signal values for both samples is challenging due to the uncalibrated variations in the tip−sample properties, the same

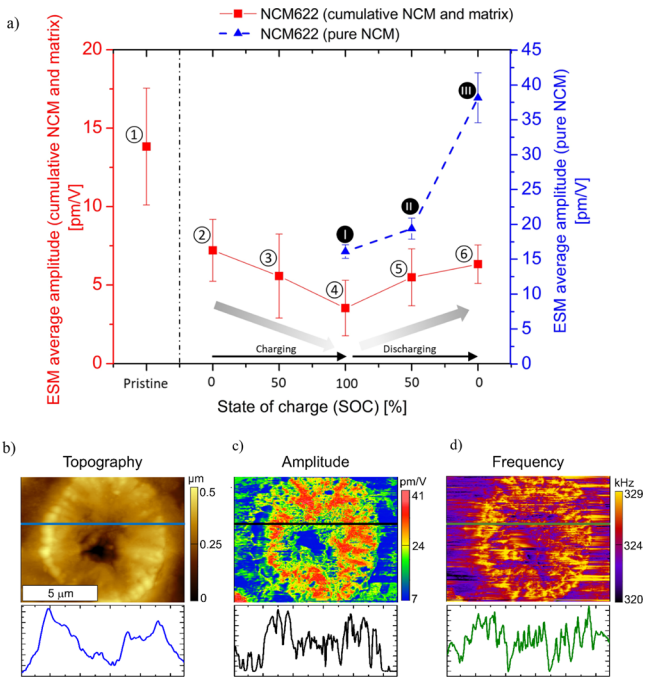

Figure 3. (a) Average ESM amplitude as a function of the SOC when charging and discharging both the pure NCM particles (blue) and cumulative NCM with a supporting matrix (red). The gray arrows are a guide for the eye, showing the decreasing or increasing ESM amplitudes. A close-up of the fully lithiated (0% SOC) NCM622 particle (b) topography, (c) ESM amplitude response, and (d) CRF and corresponding line scans.

effect might explain the overall lower ESM amplitude in the case of the cycled electrodes (②−⑥ in Figure 3). The pure NCM values (I−III in Figure 3) exhibit the same trend; however, a much stronger increase in the ESM signal is observed from 50% SOC to 0% SOC (III—in Figure 3), albeit with larger standard deviations than that with the initial 0% SOC (I in Figure 3). This behavior is also reflected in the histograms depicted in [Figures 1 and 2a(iii),b(iii)], where the range of the measured amplitude strongly decreases at these SOCs. This observation indicates the already discussed highly heterogeneous nature of the individual NCM particles. Generally, comparing the cases between cumulative (①-⑥ in Figure 3) and pure NCM (I−III in Figure 3), significantly higher standard deviations are observed on the cumulative NCM. This can be attributed to two distinct regions with the cumulative approach: hard active NCM particles and softer binder material (Figure S4). As both materials exhibit different individual ESM signals,[40] a larger variation across full ESM images can be expected compared to that with pure NCM particles.

A close-up of an individual particle at 0% SOC is shown in Figure 3b−d. Significant variations are detected inside the typical particle within the topography as well as in the ESM amplitude signal that are not directly related to each other. A closer inspection of the line sections depicted in Figure 3 indicates that elevated areas correspond to higher ESM amplitudes. Although the ESM signal is prone to be influenced by the surface topography, a direct correlation between both signals is not found, as indicated by the different shapes of the respective line sections. This is in agreement with the earlier observations of the cross-talk between the ESM signal and the sample's topography on a solid-state electrolyte.[45]

https://doi.org/10.1021/acsaem.1c03173
ACS Appl. Energy Mater. 2022, 5, 1731−1742

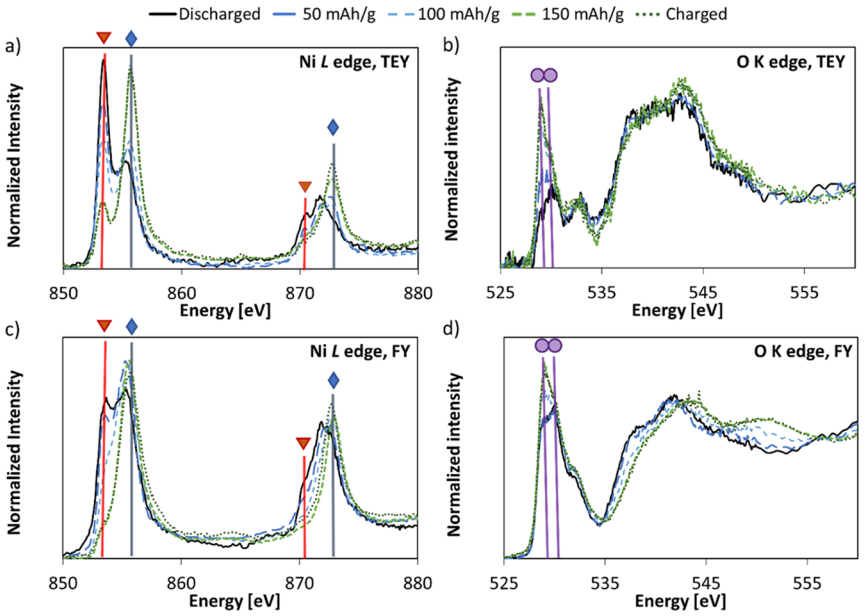

Figure 4. Ni $L_{2,3}$ edge (a,c) and O K edge (b,d) NEXAFS spectra of NCM622, measured in the discharged state (0% SOC) at 50 mA h/g (approximately 27% SOC), at 100 mA h/g (55% SOC), at 250 mA h/g (83% SOC), and in the charged state (100% SOC) using the TEY detection mode (a and b) and the FY detection mode (c and d). The probing depth of the TEY mode is ~10 nm, while the probing depth of the FY mode is a few hundreds of nanometers.

The cross-section measurements prove that the amplitude is higher at the boundary than that inside the particles, which confirms that the charge/discharge proceeds inhomogeneously across the particles, as suggested earlier.[42,43] However, lithium-depleted regions were previously located at the boundary, which would suggest that the ESM measurements are not sensitive to the Li content because the highest amplitude is observed at the boundary. Except for a region roughly in the center of the particle where ESM shows a very low signal, the particle exhibits fluctuating but rather high ESM values, as also demonstrated in Figure 2a(i).

An important observation is made with respect to the CRF shown in Figure 3d: close to the boundary of the particle with the surrounding matrix, the CRF is slightly higher, indicating a difference in the mechanical properties of the material, thereby supporting a potentially different oxidation state of the material.

Differences between the boundary and bulk chemistry of NCM622 are therefore investigated using NEXAFS spectroscopy, which was performed in the surface-sensitive total electron and the more bulk-sensitive fluorescence yield modes (TEY and FY modes). Absorption correction of the FY data was performed as described in refs 46 and 47, which allows the comparison of the relative peak intensities of the TEY and FY data. Please note that the absorption correction had minor effects on the FY spectra due to the relatively high conductive carbon content (molar ratio of carbon to the investigated element in NCM622) in the composite electrode (see the Experimental Section).

The observed peaks in the Ni L spectra (Figure 4a,c) can be assigned to ionic Ni^{2+} (>96% Ni $3d^8$ O $2p^6$ and <4% Ni $3d^9$ O $2p^5$, peaks marked with red triangles) and very covalent Ni^{3+} (approximately 30% Ni $3d^7$ O $2p^6$ and 70% Ni $3d^8$ O $2p^5$, peaks marked with blue diamonds), as revealed earlier.[39]

In the discharged state, significantly more Ni^{2+} is present on the surface (Figure 4a) than that in the bulk (Figure 4c). This implies a gradient in the electronic properties from the outside to the inside with more ionic Ni^{2+} on the surface. With the increasing SOC, the Ni^{2+} peaks decrease (red triangles), while the peaks of very covalent Ni^{3+} (blue diamonds) increase (Figure 4a,c). The electronic structure thus turns to a more covalent structure, which is confirmed by the changes at the O K edge.

With increasing covalence (Ni^{3+} configuration), the Ni−O hybrid peaks at 529 eV and 530 eV increase (Figure 4b,d, purple circles).[23,32,33] At the end of charging, the Ni^{2+}/Ni^{3+} ratios of the TEY and FY data are nearly aligned with each other, although the ratio decreases significantly upon charging in both cases (Figure 4a,c).

The observed changes are the same at the boundary and in the bulk: ionic Ni^{2+} reacts to give covalent Ni^{3+}, forming Ni−O hybrid states, as discussed in the prior report.[32] However, in the discharged state, much more Ni^{2+}, the redox active species that enables the charge transport, is present at the boundary than that in the bulk, which might explain the much higher ESM amplitude at the boundary (Figure 2a, 0% SOC). This gradient is also reflected in the observed CRF: as the bonding becomes more covalent, a stiffer region is expected at the rim of the particle, and thus, an increase in the CRF is found. With the increasing SOC, more covalent Ni^{3+}, which forces the charge carriers to stay localized, is formed, and the Ni^{2+} gradient from the boundary toward the bulk balances out. This also agrees with the ESM results since the inhomogeneity is significantly reduced at high SOCs and was found for NCA ($LiNi_{0.8}Co_{0.015}Al_{0.05}O_2$) as well.[23]

The chemical properties of NCM622, that is, its electronic structure, also correlate with the crystallographic changes, as depicted in Figure 5. The 003 and 101 reflections shifting in opposite directions (Figure 5a) imply that anisotropic changes occur in the crystallographic structure of NCM622 during delithiation/lithiation. The *a* and *b* lattice parameters decrease with an increasing SOC (Figure 5c), which is due to the increasing covalence of the Me−O bonds.[32]

https://doi.org/10.1021/acsaem.1c03173
ACS Appl. Energy Mater. 2022, 5, 1731−1742

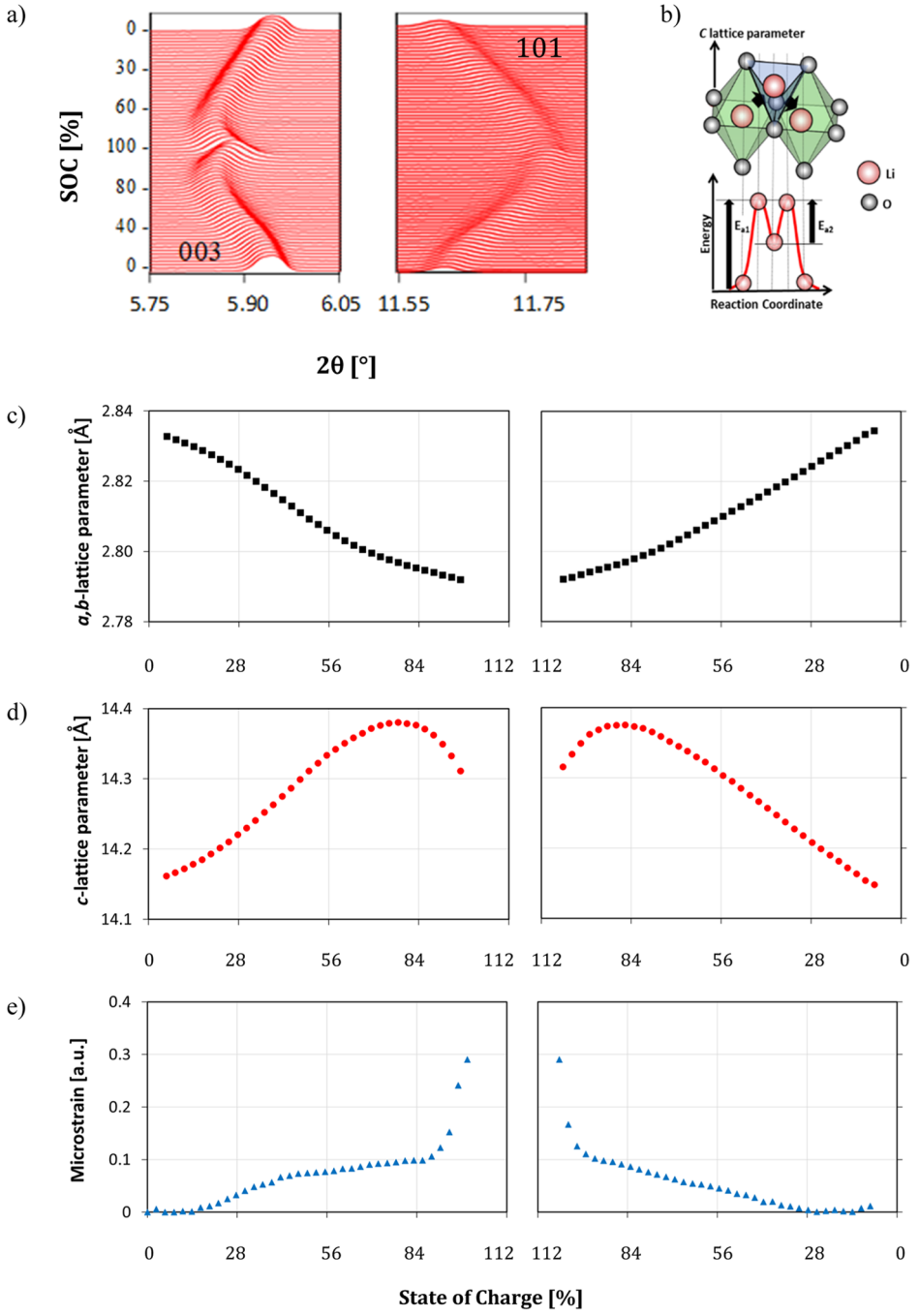

Figure 5. Powder diffraction data of NCM622: (a) operando synchrotron powder diffraction data of NCM622 during the first charge/discharge cycle, (b) the proposed Li migration mechanism in NCM622, and (c–e) changes in the *a*, *b*, and *c* lattice parameters and microstrain when charging and discharging NCM622, respectively.

Li diffusion proceeds from octahedral sites to tetrahedral sites in the Li layer (Figure 5b). The interstitial tetrahedral sites in the Li layer, namely, the attractive interactions between O and Li, determine the activation barrier of Li migration.[32,48] The smaller the tetrahedra are, the larger the attractive interactions between Li and O are, and thus, the higher the activation barrier of the migration process is. The size of the tetrahedra, in turn, is defined by the *c* lattice parameter, which increases until approximately 90% SOC (Figure 5d) and then drops at higher SOCs.[32] This agrees with the oxidation/reduction process; between 150 mA h g^{-1} and the charged state, the NEXAFS spectra hardly differ or even return, showing that there are other, probably irreversible reactions occurring (Figure 5e).[32]

While Li mobility is assumed to increase with the increasing SOC due to the increasing *c* lattice parameter, which is confirmed by the increasing (Li) diffusion coefficient (Figure S5d), the ESM amplitude decreases due to either the lower amount of Li ions present or the changes in the electronic structure (see the discussion about the NEXAFS data).

Moreover, the anisotropic lattice strain mainly observed in the *c* direction (Figure 5e) increases with the increasing SOC (in more detail, between 0 and 90% SOC), which implies a more inhomogeneous Li distribution across the particles with a

https://doi.org/10.1021/acsaem.1c03173
ACS Appl. Energy Mater. 2022, 5, 1731−1742

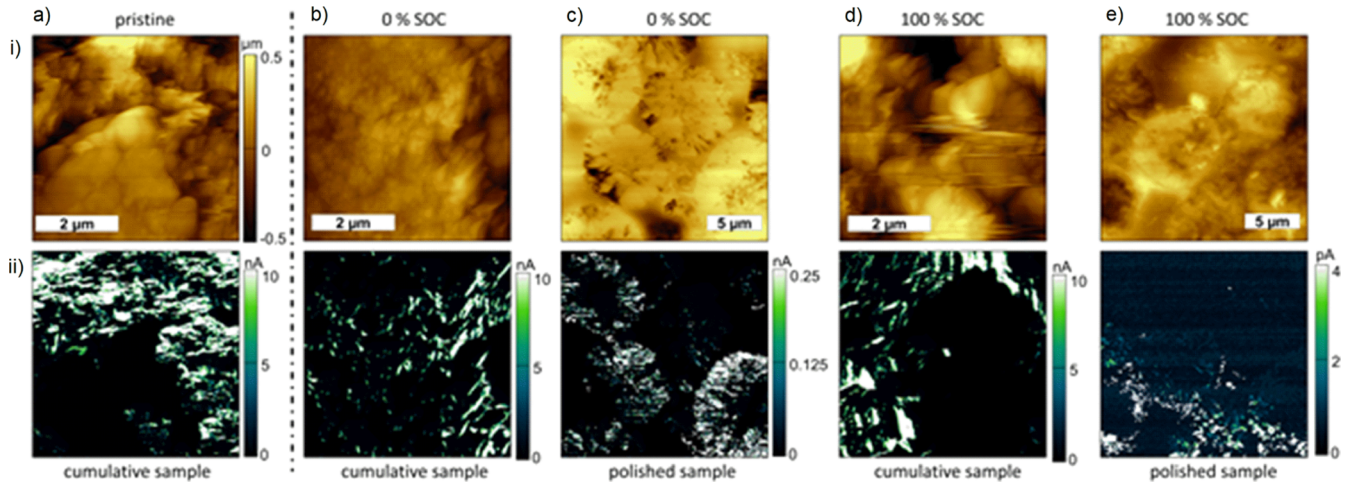

Figure 6. Topography (i) images of (a) the pristine sample and cumulative samples at (b) 0% SOC and (d) 100% SOC as well as the polished samples at (c) 0% SOC and (e) 100% SOC. (ii) Respective C-AFM images of NCM622 with a bias of 1 V (pristine and cumulative samples) or 4 V (polished samples).

lower Li content (higher SOC), as observed previously.[42,43,49] This contrasts with the ESM and NEXAFS findings, where the discussed gradient balances out with an increasing SOC. Between 90% and 100% SOC, the microstrain increases significantly, as shown in Figure 5e. Impedance spectroscopy has shown that cathode materials run into blocking conditions at these SOCs because no mobile charge carriers are present.[50] This is confirmed by the fact that at this point, the diffusion coefficient drops (Figure S5c) and the Ni^{2+} content in the bulk (*i.e.*, the redox active sites in NCM622) is suppressed to zero (Figure 4c).[23,32,33]

Given that the spatially resolved ESM measurements follow the NEXAFS data, this is a strong indication toward the conclusion that ESM is rather sensitive to the electronic structure, that is, the mobility of charge carriers, and is less likely to be directly affected by the Li distribution in electrodes.

To obtain more insights into the changes in the electronic structure of NCM622, C-AFM was performed in addition to ESM on the state-of-the-art (cumulative) electrode and the polished samples, as illustrated in Figure 6. Figure 6a shows the representative topography and C-AFM mappings of the pristine NCM622 electrode. Moreover, the obtained topography and C-AFM mappings at 0% SOC (fully lithiated) and 100% SOC (fully delithiated) are provided in Figure 6b–e for comparison.

High current signals arise from the support matrix (binder and conductive carbon), as shown in Figure 6a,b(ii), while the signal of the active material is rather low. This is in agreement with the previous studies where the conductivity of Super-P and PVDF show larger conductivities than NCM,[51,52] despite the fact that NCM, with its higher Ni content, might have even higher ionic conductivity.[53] Moreover, it is known that the electrode–electrolyte interphase is less electronically conductive;[54] thus, its presence in samples 2–6 might have affected the conductivity of the particle surface. Even though the amount of the binder and Super-P is only 5 wt %, the regions where the support matrix is present drastically contribute to the high conductivity of the cathode [Figure 6a,b,d(i),d(ii)], impressively demonstrating the importance of homogeneously embedding NCM particles in the binder/conductive carbon matrix to obtain good electronic and ionic conductivities.

To probe the C-AFM response on only the NCM622 particles, additional polished samples were analyzed, as shown in Figure 6c,e. A position in close vicinity to the current collector was chosen to improve the electric connection to the current collector. Although the obtained value is much lower than that for the unpolished samples, possibly due to the epoxy glue in which the electrode was embedded (Figure S1), a clear current signal that stems from the NCM particles is observed (Figure 6c,e).

Figure 7a illustrates the average trends of the electrical conductivities of NCM622 as a function of the SOC. A clear relation between the SOC and average current by C-AFM is observed for both samples, that is, including and excluding the effects of the binder and Super-P.

With a decreasing SOC and an increasing degree of lithiation, the average current in the measured areas increase. Thus, it can be concluded that the electronic conductivity decreases upon charging because the NCM particles become more covalent. This argument agrees with the NEXAFS results.

Furthermore, larger parts of the NCM particles exhibit a current signal in the fully lithiated (discharged) state (SOC 0%). With the decreasing Li content, the areas of high electronic conductivity decrease. This observation is also attributed to the changes in the electronic structure of the material as a function of the SOC, as probed by NEXAFS spectroscopy and discussed earlier in this article.

Importantly, the current signal within the NCM particles is not uniform but reminiscent of the ESM results of ionic conductivity, showing a more pronounced signal at the boundary of the particle than that at the center. This inhomogeneous distribution of electronic conductivity within the individual particles additionally points to a strong correlation between the electronic state and conductivity of the material.

To rule out an experimental artifact, C-AFM and ESM were conducted at identical positions of the polished sample at 0% SOC, as shown in Figure 7b. The overlapping region is indicated by a dashed red line.

Although the overall ESM and C-AFM signal distributions within a single particle are similar, clear differences are found. In particular, a difference is found at the boundary between the particle and binder/conductive carbon matrix, where high

https://doi.org/10.1021/acsaem.1c03173
ACS Appl. Energy Mater. 2022, 5, 1731–1742

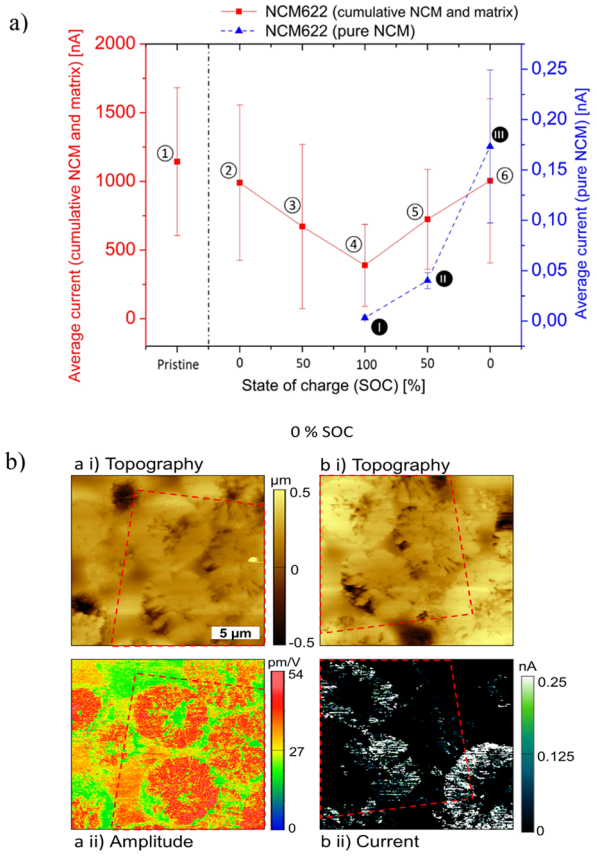

Figure 7. (a) Plot of the average current with respect to the SOC. The current was averaged over the whole image of the cumulative samples of active material and the supporting matrix, whereas it was averaged for the visible NCM particles in the case of the polished samples. (b) Comparison between the ESM and C-AFM images of the same area (marked with a slashed red line), where a(i) and a(ii) are the simultaneously obtained topography and ESM images and b(i) and b(ii) are the simultaneously obtained topography and C-AFM images, respectively.

ESM values are found, while the C-AFM signal fluctuates. Additionally, one of the particles [right-hand side in Figure 7a,b(ii)] shows a clear ESM response but appears to have either lost its electronic connection or is indeed locally less conductive. It can be concluded that in addition to the inhomogeneous delithiation, as already discussed in the literature,[35,42,43,49] the electronic conductivity varies strongly within the samples. Both effects can be traced back to local variations in the material composition, leading to deviations in the Li-ion transport resistance and electronic state.

In summary, the C-AFM and NEXAFS results indicate a stronger covalent bonding situation in the case of delithiated (charged) NCM622, leading to the decreasing current and Ni^{2+} content with the increasing SOC. Consequently, the ESM amplitude and C-AFM values mainly respond to the local oxidation state and bonding conditions of the Me−O host structure, especially when the SOC is close to 100%. These key observations and findings from all the discussed techniques are summarized in Table 1.

This explanation is further supported when calculating the Li-ion diffusion length based on the Li diffusion constant of $\sim 10^3$ nm^2 s^{-1} for 100% SOC (Figure S5) and an applied AC frequency, which is on the order of 320 kHz. As a result, a movement of only ∼0.05−0.06 nm is expected per alternating field, which is far below the lattice constant of NCM; thus, the typically applied Vegard strain mechanism of ESM is a minor source of the amplitude signal in this system.

4. CONCLUSIONS

ESM and C-AFM were applied on state-of-the-art NCM622 electrodes, and spatially resolved studies were performed on polished NCM622 surfaces. Furthermore, the SOC-dependent chemical composition and crystallographic structure were investigated using NEXAFS spectroscopy and powder diffraction. With this correlative approach, it was demonstrated that there was a gradient in the chemical composition and electronic properties of NCM622 particles from the boundaries toward the bulk, which was more pronounced in the discharged state and balanced out when charging. While the ESM signal was found to be proportional to the overall Li content and thus to the SOC of the material, a closer inspection revealed that the origin of the observed ESM amplitude and the trends when charging and discharging can be related to the electronic configuration of Ni, which promoted or inhibited the charge transfer. Therefore, a direct correlation between the ESM signal and the amount of Li ions present in the structure was restricted.

In summary, this work contributes to the understanding of the local electrochemical and electrical phenomena, the origin of microscopic changes at different SOCs, and the interplay between the electronic/ionic conductivities and crystallographic structures. These findings can point toward further quantitative analysis of the ESM results, which will help design, optimize, and improve electrodes for future Li-ion batteries by improving the understanding of the chemical and physical processes at multiple scales. The results can guide future

Table 1. Summative Observations

section	key findings
ESM	ESM amplitude has a strong negative correlation with the NCM622 SOC, which is attributed to the changes in the local electronic structure of the Me−O host and the resulting mobility of charge carriers.
NEXAFS	Ionic Ni^{2+} reacts to give Ni^{3+} upon charge (increase of the SOC in NCMs) while forming covalent bonds to its oxygen neighbors. This forces the charge carriers to stay localized and reduces the ESM amplitude. The Ni^{2+}/Ni^{3+} gradient across the particle balances out with the increasing SOC.
XRD	The *a* and *b* lattice parameters decrease with the increasing SOC, which is due to the increasing covalence of the Me−O bonds. The anisotropic lattice strain mainly observed in the *c* direction increases with the higher SOC, which implies a more inhomogeneous Li distribution across the particles with a lower Li content, contrasting with the ESM results.
C-AFM	With a higher SOC, the average current in the measured areas of NCM622 reduces. The electronic conductivity decreases as the NCM particles become more covalent. This observation agrees with the NEXAFS results.
Overall	Although the Vegard strain is not the dominant mechanism for the observed ESM amplitude, ESM is successfully applied to study the system. As the ESM signal is in accordance with the NEXAFS data but in contrast to the effect of the *c*-lattice parameter, ESM rather probes the Li-ion mobility than the local Li distribution in the system.

https://doi.org/10.1021/acsaem.1c03173
ACS Appl. Energy Mater. 2022, 5, 1731−1742

macro- and nanoscale engineering of Li-ion batteries and gas sensors that require high precision and accuracy of the electrochemical strain and delithiation/lithiation estimations. Finally, the further comprehension and development of AFM techniques will allow *operando* experiments to be performed and "online" chemical reactions and changes in battery properties to be studied.

■ ASSOCIATED CONTENT

Supporting Information

The Supporting Information is available free of charge at https://pubs.acs.org/doi/10.1021/acsaem.1c03173.

Additional details on the sample preparation and the GITT results (PDF)

■ AUTHOR INFORMATION

Corresponding Authors

Karin Kleiner − *Münster Electrochemical Energy Technology (MEET), University of Münster, Münster 48149, Germany*; Email: karin.kleiner@uni-muenster.de

Florian Hausen − *Forschungszentrum Jülich, Institute of Energy and Climate Research, Jülich 52428, Germany; Institute of Physical Chemistry, RWTH Aachen University, Aachen 52074, Germany*; orcid.org/0000-0001-5712-6761; Email: f.hausen@fz-juelich.de

Seungbum Hong − *Department of Materials Science and Engineering, Korea Advanced Institute of Science and Technology (KAIST), Daejeon 34141, Republic of Korea; KAIST Institute for the NanoCentury, KAIST, Daejeon 34141, Republic of Korea*; orcid.org/0000-0002-2667-1983; Email: seungbum@kaist.ac.kr

Authors

Albina Jetybayeva − *Department of Materials Science and Engineering, Korea Advanced Institute of Science and Technology (KAIST), Daejeon 34141, Republic of Korea*; orcid.org/0000-0002-0652-3756

Nino Schön − *Forschungszentrum Jülich, Institute of Energy and Climate Research, Jülich 52428, Germany; Institute of Physical Chemistry, RWTH Aachen University, Aachen 52074, Germany*

Jimin Oh − *Department of Materials Science and Engineering, Korea Advanced Institute of Science and Technology (KAIST), Daejeon 34141, Republic of Korea; Electronics and Telecommunications Research Institute (ETRI), Daejeon 34129, Korea*; orcid.org/0000-0002-5770-0863

Jaegyu Kim − *Department of Materials Science and Engineering, Korea Advanced Institute of Science and Technology (KAIST), Daejeon 34141, Republic of Korea*

Hongjun Kim − *Department of Materials Science and Engineering, Korea Advanced Institute of Science and Technology (KAIST), Daejeon 34141, Republic of Korea*; orcid.org/0000-0002-2689-9769

Gun Park − *Department of Materials Science and Engineering, Korea Advanced Institute of Science and Technology (KAIST), Daejeon 34141, Republic of Korea*; orcid.org/0000-0003-2496-3656

Young-Gi Lee − *Electronics and Telecommunications Research Institute (ETRI), Daejeon 34129, Korea*; orcid.org/0000-0002-6364-4626

Rüdiger-A. Eichel − *Forschungszentrum Jülich, Institute of Energy and Climate Research, Jülich 52428, Germany; Institute of Physical Chemistry, RWTH Aachen University, Aachen 52074, Germany*; orcid.org/0000-0002-0013-6325

Complete contact information is available at: https://pubs.acs.org/10.1021/acsaem.1c03173

Author Contributions

¶These authors contributed equally.

Notes

The authors declare no competing financial interest.

■ ACKNOWLEDGMENTS

A.J. and N.S. contributed equally to the work described in this manuscript. We thank Dr. George W. Crabtree at the Argonne National Laboratory for his advice and fruitful discussion. The work from Korea was supported by the KAIST-funded Global Singularity Research Program for 2020, 2021, and 2022; the Big Sciences Research Program (no. 2017M1A2A2044498) through the National Research Foundation of Korea (NRF), funded by the Ministry of Science and ICT; and the Wearable Platform Materials Technology Center (WMC), funded by the NRF Grant by the Korean Government (MSIT) (no. 2016R1A5A1009926). We also wish to acknowledge KARA, the KNMF (both Karlsruhe, Germany), and the Diamond Light Source (UK, proposal NR19772) for the provision of beamtime. The NEXAFS and diffraction studies were supported by the Federal Ministry of Education and Research under grant number 03XP0231, and the author is responsible for the content of this publication.

■ REFERENCES

(1) Gür, T. M. Review of Electrical Energy Storage Technologies, Materials and Systems: Challenges and Prospects for Large-Scale Grid Storage. *Energy Environ. Sci.* **2018**, *11*, 2696−2767.

(2) Goldie-Scot, L. *Electric Vehicles: The End of the Beginning; 03.-05.11.2020: AABC Virtual*; Bloomberg New Energy Finance Head of Clean Power, 2020.

(3) Bernhart, W. *Lithium-Ion Batteries − New Business Models Emerging; 03.-05.11.2020: AABC Virtual*; Roland Berger Strategy Consultants GmbH Sr Partner, 2020.

(4) Andre, D.; Kim, S.-J.; Lamp, P.; Lux, S. F.; Maglia, F.; Paschos, O.; Stiaszny, B. Future Generations of Cathode Materials: An Automotive Industry Perspective. *J. Mater. Chem. A* **2015**, *3*, 6709−6732.

(5) Kleiner, K.; Ehrenberg, H. Challenges Considering the Degradation of Cell Components in Commercial Lithium-Ion Cells: A Review and Evaluation of Present Systems. *Top. Curr. Chem.* **2017**, *375*, 45.

(6) Hong, S.; Liow, C. H.; Yuk, J. M.; Byon, H. R.; Yang, Y.; Cho, E.; Yeom, J.; Park, G.; Kang, H.; Kim, S.; Shim, Y.; Na, M.; Jeong, C.; Hwang, G.; Kim, H.; Kim, H.; Eom, S.; Cho, S.; Jun, H.; Lee, Y.; Baucour, A.; Bang, K.; Kim, M.; Yun, S.; Ryu, J.; Han, Y.; Jetybayeva, A.; Choi, P.-P.; Agar, J. C.; Kalinin, S. V.; Voorhees, P. W.; Littlewood, P.; Lee, H. M. Reducing Time to Discovery: Materials and Molecular Modeling, Imaging, Informatics, and Integration. *ACS Nano* **2021**, *15*, 3971−3995.

(7) Myung, S.-T.; Maglia, F.; Park, K.-J.; Yoon, C. S.; Lamp, P.; Kim, S.-J.; Sun, Y.-K. Nickel-Rich Layered Cathode Materials for Automotive Lithium-Ion Batteries: Achievements and Perspectives. *ACS Energy Lett.* **2017**, *2*, 196−223.

(8) De Biasi, L.; Kondrakov, A. O.; Geßwein, H.; Brezesinski, T.; Hartmann, P.; Janek, J. Between Scylla and Charybdis: Balancing among Structural Stability and Energy Density of Layered NCM Cathode Materials for Advanced Lithium-Ion Batteries. *J. Phys. Chem. C* **2017**, *121*, 26163−26171.

(9) Jung, R.; Metzger, M.; Maglia, F.; Stinner, C.; Gasteiger, H. A. Oxygen Release and Its Effect on the Cycling Stability of LiNixMnyCozO2(NMC) Cathode Materials for Li-Ion Batteries. *J. Electrochem. Soc.* **2017**, *164*, A1361−A1377.
(10) Schweidler, S.; de Biasi, L.; Garcia, G.; Mazilkin, A.; Hartmann, P.; Brezesinski, T.; Janek, J. Investigation into Mechanical Degradation and Fatigue of High-Ni NCM Cathode Material: A Long-Term Cycling Study of Full Cells. *ACS Appl. Energy Mater.* **2019**, *2*, 7375−7384.
(11) Neudeck, S.; Walther, F.; Bergfeldt, T.; Suchomski, C.; Rohnke, M.; Hartmann, P.; Janek, J.; Brezesinski, T. Molecular Surface Modification of NCM622 Cathode Material Using Organophosphates for Improved Li-Ion Battery Full-Cells. *ACS Appl. Mater. Interfaces* **2018**, *10*, 20487−20498.
(12) Qian, K.; Huang, B.; Liu, Y.; Wagemaker, M.; Liu, M.; Duan, H.; Liu, D.; He, Y.-B.; Li, B.; Kang, F. Increase and discretization of the energy barrier for individual LiNixCoyMnyO2 (x + 2y =1) particles with the growth of a Li2CO3 surface film. *J. Mater. Chem. A* **2019**, *7*, 12723−12731.
(13) Evertz, M.; Kasnatscheew, J.; Winter, M.; Nowak, S. Investigation of Various Layered Lithium Ion Battery Cathode Materials by Plasma- and X-Ray-Based Element Analytical Techniques. *Anal. Bioanal. Chem.* **2019**, *411*, 277−285.
(14) Xu, L.; Zhou, F.; Liu, B.; Zhou, H.; Zhang, Q.; Kong, J.; Wang, Q. Progress in Preparation and Modification of $LiNi_{0.6}Mn_{0.2}Co_{0.2}O_2$ Cathode Material for High Energy Density Li-Ion Batteries. *Int. J. Electrochem.* **2018**, *2018*, 1−12.
(15) Wang, D.; Li, X.; Wang, W.; Wang, Z.; Guo, H.; Ru, J. Improvement of High Voltage Electrochemical Performance of $LiNi_{0.5}Co_{0.2}Mn_{0.3}O_2$ Cathode Materials via Li_2ZrO_3 Coating. *Ceram. Int.* **2015**, *41*, 6663−6667.
(16) Cui, S.; Wei, Y.; Liu, T.; Deng, W.; Hu, Z.; Su, Y.; Li, H.; Li, M.; Guo, H.; Duan, Y.; Wang, W.; Rao, M.; Zheng, J.; Wang, X.; Pan, F. Optimized Temperature Effect of Li-Ion Diffusion with Layer Distance in $Li(Ni_xMn_yCo_z)O_2$ Cathode Materials for High Performance Li-Ion Battery. *Adv. Energy Mater.* **2016**, *6*, 1501309.
(17) Fellner, J. P.; Loeber, G. J.; Sandhu, S. S. Testing of Lithium-Ion 18650 Cells and Characterizing/Predicting Cell Performance. *J. Power Sources* **1999**, *81*−*82*, 867−871.
(18) Nickol, A.; Schied, T.; Heubner, C.; Schneider, M.; Michaelis, A.; Bobeth, M.; Cuniberti, G. GITT Analysis of Lithium Insertion Cathodes for Determining the Lithium Diffusion Coefficient at Low Temperature: Challenges and Pitfalls. *J. Electrochem. Soc.* **2020**, *167*, 090546.
(19) Weppner, W.; Huggins, R. a. Electrochemical Methods for Determining Kinetic Properties of Solids. *Annu. Rev. Mater. Sci.* **1978**, *8*, 269−311.
(20) Purushothaman, B. K.; Landau, U. Rapid Charging of Lithium-Ion Batteries Using Pulsed Currents. *J. Electrochem. Soc.* **2006**, *153*, A533−A542.
(21) Amalraj, F.; Talianker, M.; Markovsky, B.; Sharon, D.; Burlaka, L.; Shafir, G.; Zinigrad, E.; Haik, O.; Aurbach, D.; Lampert, J.; Schulz-Dobrick, M.; Garsuch, A. Study of the Lithium-Rich Integrated Compound xLi2MnO3·(1-x)LiMO2(x around 0.5; M = Mn, Ni, Co; 2:2:1) and Its Electrochemical Activity as Positive Electrode in Lithium Cells. *J. Electrochem. Soc.* **2013**, *160*, A324−A337.
(22) Montoro, L. A.; Rosolen, J. M. The Role of Structural and Electronic Alterations on the Lithium Diffusion in LixCo0.5Ni0.5O2. *Electrochim. Acta* **2004**, *49*, 3243−3249.
(23) Kleiner, K.; Melke, J.; Merz, M.; Jakes, P.; Nagel, P.; Schuppler, S.; Liebau, V.; Ehrenberg, H. Unraveling the Degradation Process of LiNi0.8Co0.15Al0.05O2 Electrodes in Commercial Lithium Ion Batteries by Electronic Structure Investigations. *ACS Appl. Mater. Interfaces* **2015**, *7*, 19589−19600.
(24) Kalinin, S. V.; Dyck, O.; Balke, N.; Neumayer, S.; Tsai, W.-Y.; Vasudevan, R.; Lingerfelt, D.; Ahmadi, M.; Ziatdinov, M.; McDowell, M. T.; Strelcov, E. Toward Electrochemical Studies on the Nanometer and Atomic Scales: Progress, Challenges, and Opportunities. *ACS Nano* **2019**, *13*, 9735−9780.
(25) Li, T.; Zeng, K. Probing of Local Multifield Coupling Phenomena of Advanced Materials by Scanning Probe Microscopy Techniques. *Adv. Mater.* **2018**, *30*, 1803064.
(26) Kim, H.; Oh, J.; Park, G.; Jetybayeva, A.; Kim, J.; Lee, Y.-G.; Hong, S. Visualization of Functional Components in a Lithium Silicon Titanium Phosphate-Natural Graphite Composite Anode. *ACS Appl. Energy Mater.* **2020**, *3*, 3253−3261.
(27) Balke, N.; Jesse, S.; Kim, Y.; Adamczyk, L.; Tselev, A.; Ivanov, I. N.; Dudney, N. J.; Kalinin, S. V. Real Space Mapping of Li-Ion Transport in Amorphous Si Anodes with Nanometer Resolution. *Nano Lett.* **2010**, *10*, 3420−3425.
(28) Balke, N.; Kalnaus, S.; Dudney, N. J.; Daniel, C.; Jesse, S.; Kalinin, S. V. Local Detection of Activation Energy for Ionic Transport in Lithium Cobalt Oxide. *Nano Lett.* **2012**, *12*, 3399−3403.
(29) Yang, S.; Yan, B.; Li, T.; Zhu, J.; Lu, L.; Zeng, K. In Situ Studies of Lithium-Ion Diffusion in a Lithium-Rich Thin Film Cathode by Scanning Probe Microscopy Techniques. *Phys. Chem. Chem. Phys.* **2015**, *17*, 22235−22242.
(30) Alikin, D. O.; Romanyuk, K. N.; Slautin, B. N.; Rosato, D.; Shur, V. Y.; Kholkin, A. L. Quantitative Characterization of the Ionic Mobility and Concentration in Li-Battery Cathodes via Low Frequency Electrochemical Strain Microscopy. *Nanoscale* **2018**, *10*, 2503−2511.
(31) Lanza, M. *Conductive Atomic Force Microscopy*, 1st ed.; Lanza, M., Ed.; Wiley-VCH Verlag GmbH & Co. KGaA: Weinheim, Germany, 2017.
(32) Kleiner, K.; Murray, C. A.; Grosu, C.; Ying, B.; Winter, M.; Nagel, P.; Schuppler, S.; Merz, M. On the Origin of Reversible and Irreversible Reactions in $LiNi_xCo_{(1-x)/2}Mn_{(1-x)/2}O_2$. *J. Electrochem. Soc.* **2021**, *168*, 120533.
(33) Merz, M.; Ying, B.; Nagel, P.; Schuppler, S.; Kleiner, K. Reversible and Irreversible Redox Processes in Li-Rich Layered Oxides. *Chem. Mater.* **2021**, *33*, 9534−9545.
(34) Strelcov, E.; Yang, S. M.; Jesse, S.; Balke, N.; Vasudevan, R. K.; Kalinin, S. V. Solid-State Electrochemistry on the Nanometer and Atomic Scales: The Scanning Probe Microscopy Approach. *Nanoscale* **2016**, *8*, 13838−13858.
(35) Alikin, D. O.; Ievlev, A. V.; Luchkin, S. Y.; Turygin, A. P.; Shur, V. Y.; Kalinin, S. V.; Kholkin, A. L. Characterization of $LiMn_2O_4$ Cathodes by Electrochemical Strain Microscopy. *Appl. Phys. Lett.* **2016**, *108*, 113106.
(36) Park, G.; Kim, H.; Oh, J.; Choi, Y.; Ovchinnikova, O. S.; Min, S.; Lee, Y.-G.; Hong, S. Quantitative Measurement of Li-Ion Concentration and Diffusivity in Solid-State Electrolyte. *ACS Appl. Energy Mater.* **2021**, *4*, 784−790.
(37) Schön, N.; Schierholz, R.; Jesse, S.; Yu, S.; Eichel, R. A.; Balke, N.; Hausen, F. Signal Origin of Electrochemical Strain Microscopy and Link to Local Chemical Distribution in Solid State Electrolytes. *Small Methods* **2021**, *5*, 2001279.
(38) Edström, K.; Gustafsson, T.; Thomas, J. O. The cathode-electrolyte interface in the Li-ion battery. *Electrochim. Acta* **2004**, *50*, 397−403.
(39) Zheng, Y.; Xu, N.; Chen, S.; Liao, Y.; Zhong, G.; Zhang, Z.; Yang, Y. Construction of a Stable $LiNi_{0.8}Co_{0.1}Mn_{0.1}O_2$ (NCM811) Cathode Interface by a Multifunctional Organosilicon Electrolyte Additive. *ACS Appl. Energy Mater.* **2020**, *3*, 2837−2845.
(40) Zhu, J.; Lu, L.; Zeng, K. Nanoscale Mapping of Lithium-Ion Diffusion in a Cathode within an All-Solid-State Lithium-Ion Battery by Advanced Scanning Probe Microscopy Techniques. *ACS Nano* **2013**, *7*, 1666−1675.
(41) Seol, D.; Seo, H.; Jesse, S.; Kim, Y. Nanoscale Mapping of Electromechanical Response in Ionic Conductive Ceramics with Piezoelectric Inclusions. *J. Appl. Phys.* **2015**, *118*, 072014.
(42) Kleiner, K.; Dixon, D.; Jakes, P.; Melke, J.; Yavuz, M.; Roth, C.; Nikolowski, K.; Liebau, V.; Ehrenberg, H. Fatigue of $LiNi_{0.8}Co_{0.15}Al_{0.05}O_2$ in Commercial Li Ion Batteries. *J. Power Sources* **2015**, *273*, 70−82.
(43) De Biasi, L.; Schwarz, B.; Brezesinski, T.; Hartmann, P.; Janek, J.; Ehrenberg, H. Chemical, Structural, and Electronic Aspects of

https://doi.org/10.1021/acsaem.1c03173
ACS Appl. Energy Mater. 2022, 5, 1731−1742

Formation and Degradation Behavior on Different Length Scales of Ni-Rich NCM and Li-Rich HE-NCM Cathode Materials in Li-Ion Batteries. *Adv. Mater.* **2019**, *31*, 1900985.
(44) Darma, M. S. D.; Lang, M.; Kleiner, K.; Mereacre, L.; Liebau, V.; Fauth, F.; Bergfeldt, T.; Ehrenberg, H. The Influence of Cycling Temperature and Cycling Rate on the Phase Specific Degradation of a Positive Electrode in Lithium Ion Batteries: A Post Mortem Analysis. *J. Power Sources* **2016**, *327*, 714−725.
(45) Schön, N.; Gunduz, D. C.; Yu, S.; Tempel, H.; Schierholz, R.; Hausen, F. Correlative Electrochemical Strain and Scanning Electron Microscopy for Local Characterization of the Solid State Electrolyte $Li_{1.3}Al_{0.3}Ti_{1.7}(PO_4)_3$. *Beilstein J. Nanotechnol.* **2018**, *9*, 1564−1572.
(46) Merz, M.; Fuchs, D.; Assmann, A.; Uebe, S.; Löhneysen, H.; Schuppler, S.; Schuppler, S. Spin and orbital states in single-layered La2−xCaxCoO4studied by doping- and temperature-dependent near-edge x-ray absorption fine structure. *Phys. Rev. B* **2011**, *84*, 014436.
(47) Merz, M.; Nagel, P.; Pinta, C.; Samartsev, A.; Löhneysen, H.; Uebe, S.; Assmann, A.; Fuchs, D.; Schuppler, S.; Schuppler, S. X-Ray Absorption and Magnetic Circular Dichroism of $LaCoO_3$, $La_{0.7}Ce_{0.3}CoO_3$, and $La_{0.7}Sr_{0.3}CoO_3$ Films: Evidence for Cobalt-Valence-Dependent Magnetism. *Phys. Rev. B* **2010**, *82*, 174416.
(48) Märker, K.; Reeves, P. J.; Xu, C.; Griffith, K. J.; Grey, C. P. Evolution of Structure and Lithium Dynamics in $LiNi_{0.8}Mn_{0.1}Co_{0.1}O_2$ (NMC811) Cathodes during Electrochemical Cycling. *Chem. Mater.* **2019**, *31*, 2545−2554.
(49) Kondrakov, A. O.; Schmidt, A.; Xu, J.; Geßwein, H.; Mönig, R.; Hartmann, P.; Sommer, H.; Brezesinski, T.; Janek, J. Anisotropic Lattice Strain and Mechanical Degradation of High- and Low-Nickel NCM Cathode Materials for Li-Ion Batteries. *J. Phys. Chem. C* **2017**, *121*, 3286−3294.
(50) Oswald, S.; Pritzl, D.; Wetjen, M.; Gasteiger, H. A. Novel Method for Monitoring the Electrochemical Capacitance by In Situ Impedance Spectroscopy as Indicator for Particle Cracking of Nickel-Rich NCMs: Part I. Theory and Validation. *J. Electrochem. Soc.* **2020**, *167*, 100511.
(51) Pantea, D.; Darmstadt, H.; Kaliaguine, S.; Roy, C. Electrical Conductivity of Conductive Carbon Blacks: Influence of Surface Chemistry and Topology. *Appl. Surf. Sci.* **2003**, *217*, 181−193.
(52) Rey-Raap, N.; Calvo, E. G.; Bermúdez, J. M.; Cameán, I.; García, A. B.; Menéndez, J. A.; Arenillas, A. An Electrical Conductivity Translator for Carbons. *Measurement* **2014**, *56*, 215−218.
(53) Amin, R.; Chiang, Y.-M. Characterization of Electronic and Ionic Transport in $Li_{1-x}Ni_{0.33}Mn_{0.33}Co_{0.33}O_2$ (NMC 333) and $Li_{1-x}Ni_{0.50}Mn_{0.20}Co_{0.30}O_2$ (NMC 523) as a Function of Li Content. *J. Electrochem. Soc.* **2016**, *163*, A1512−A1517.
(54) An, S. J.; Li, J.; Daniel, C.; Mohanty, D.; Nagpure, S.; Wood, D. L. The State of Understanding of the Lithium-Ion-Battery Graphite Solid Electrolyte Interphase (SEI) and Its Relationship to Formation Cycling. *Carbon* **2016**, *105*, 52−76.

https://doi.org/10.1021/acsaem.1c03173
ACS Appl. Energy Mater. 2022, 5, 1731−1742